Volume 13
Number 44
28 November 2021
Pages 18377-18802

Nanoscale

rsc.li/nanoscale

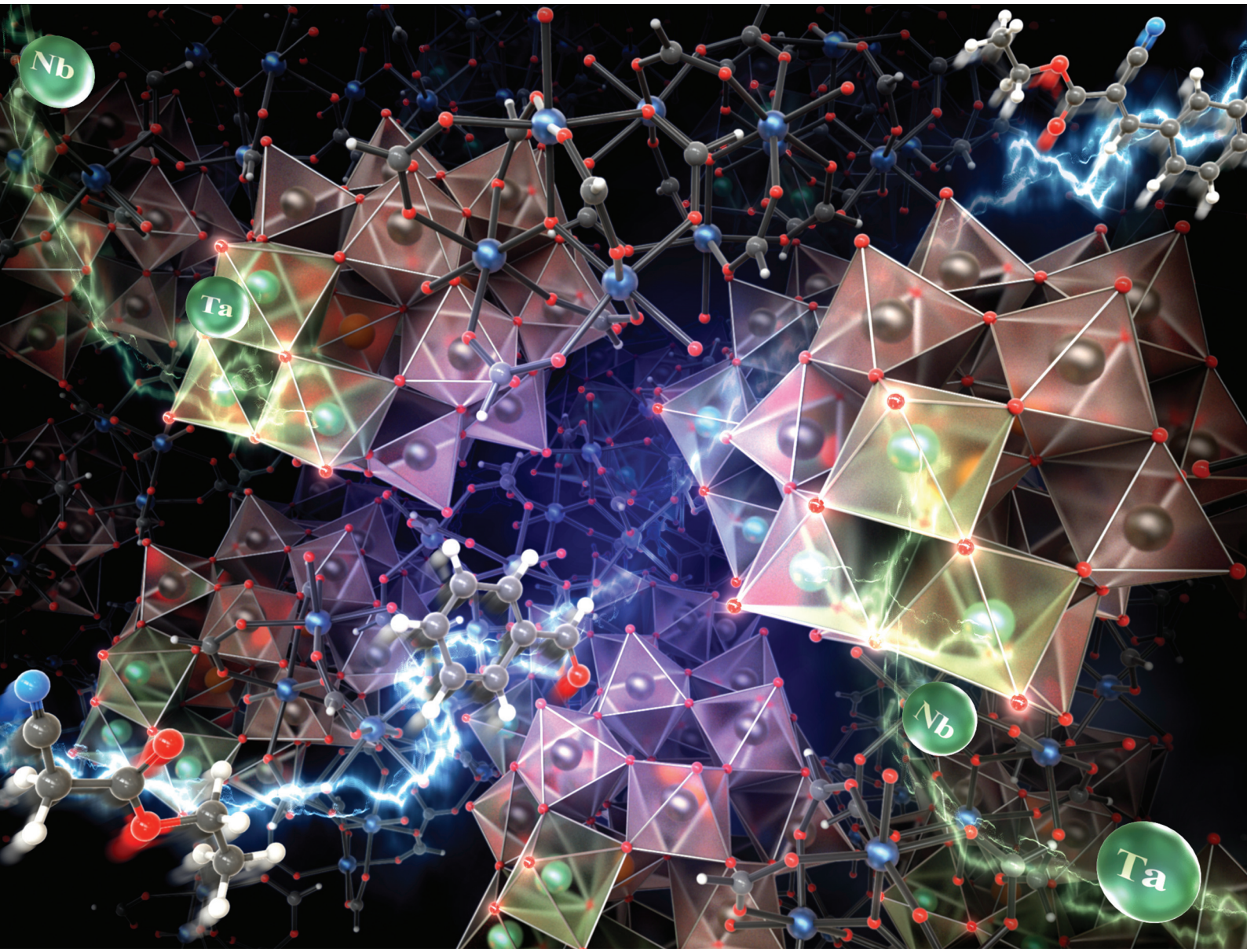

ISSN 2040-3372

ROYAL SOCIETY OF CHEMISTRY

PAPER
Sayaka Uchida *et al.*
Incorporating highly basic polyoxometalate anions comprising Nb or Ta into nanoscale reaction fields of porous ionic crystals

NCNST

Nanoscale

PAPER

View Article Online
View Journal | View Issue

Cite this: *Nanoscale*, 2021, **13**, 18451

Incorporating highly basic polyoxometalate anions comprising Nb or Ta into nanoscale reaction fields of porous ionic crystals†

Zhewei Weng,[a] Naoki Ogiwara, [a] Takashi Kitao, [b,c] Yuji Kikukawa, [d] Yu Gao,[e] Likai Yan [e] and Sayaka Uchida *[a]

Polyoxometalates (POMs) are oxide cluster anions composed of high-valence early transition metals and are widely used as catalysts. Yet base catalysis of POMs remains an ongoing challenge; group V (V, Nb, and Ta) elements form more negatively charged POMs than group VI (Mo and W) elements, and in particular, polyoxoniobates and polyoxotantalates are known to show strong basicity in solution due to the highly negative surface oxygen atoms. Herein, we report for the first time porous ionic crystals (PICs) comprising Nb or Ta. The PICs are composed of Dawson-type Nb/W or Ta/W mixed-addenda POMs with oxo-centered trinuclear Cr^{III} carboxylates and potassium ions as counter cations to control the crystal structure. Among the PICs, those with Nb or Ta tri-substituted POMs exhibit the highest yield (78–82%) and selectivity (99%) towards the Knoevenagel condensation of benzaldehyde and ethyl cyanoacetate (353 K, 6 h), which is a typical base-catalyzed reaction, as reusable solid catalysts, and they can also catalyze the reaction of other active methylene compounds. A detailed investigation into the crystal structures together with DFT calculations and *in situ* IR spectroscopy with methanol as a basic probe molecule shows that the exposure of $[Nb_3O_{13}]$ or $[Ta_3O_{13}]$ units with highly negative surface oxygen atoms to the pore surface of PICs is crucial to the catalytic performance. These findings based on the composition–structure–function relationships show that Nb- and Ta-containing PICs can serve as platforms for rational designing of heterogeneous base catalysts.

Received 22nd July 2021,
Accepted 1st October 2021

DOI: 10.1039/d1nr04762k

rsc.li/nanoscale

Introduction

Polyoxometalates (POMs) are robust, discrete, and structurally well-defined oxide cluster anions mainly composed of high-valence early transition metals.[1–3] POMs are widely used as acid catalysts,[4] oxidation catalysts,[5] and photocatalysts,[6] while base catalysis of POMs remains an ongoing challenge. It has been known that structurally and electronically well-defined surface basic oxygen atoms of POMs can abstract protons (Brønsted base) and/or act as a nucleophile (Lewis base).[7] In this context, $[WO_4]^{2-}$ shows high catalytic activity in CO_2 fixation,[8,9] and a Keggin-type lacunary POM ($[\gamma\text{-}H_2GeW_{10}O_{36}]^{6-}$) catalyzes the Knoevenagel reaction,[10] which forms C–C bonds *via* the condensation of carbonyl compounds with active methylene compounds.[11] Meanwhile, highly negatively charged POMs can act as strong base catalysts because the surface oxygen atoms generally become more basic by increasing the negative charges.[12,13] Notably, group V elements (V, Nb, and Ta) form more negatively charged POMs than group VI elements (Mo and W) due to the difference in their highest oxidation states. In particular, polyoxoniobates and polyoxotantalates show potential applications in base-catalyzed reactions.[14,15]

Counter cations are imperative to isolate and crystallize POMs,[16] and the use of metal ions has enabled breakthroughs in the formation of functional POM-based solids.[17–21] We have been working on the synthesis of porous ionic crystals (PICs), which are crystalline porous composites of POMs with molecular cations (macrocations) such as the oxo-centered trinuclear metal carboxylates with a general formula of

[a]*Department of Basic Science, School of Arts and Sciences, The University of Tokyo, Komaba, Meguro-ku, Tokyo 153-8902, Japan. E-mail: csayaka@g.ecc.u-tokyo.ac.jp*
[b]*Department of Applied Chemistry, Graduate School of Engineering, The University of Tokyo, 7-3-1 Hongo, Bunkyo-ku, Tokyo 113-8656, Japan*
[c]*Department of Advanced Materials Science, Graduate School of Frontier Sciences, The University of Tokyo, 5-1-5 Kashiwanoha, Kashiwa, Chiba 277-8561, Japan*
[d]*Department of Chemistry, Graduate School of Natural Science and Technology, Kanazawa University, Kakuma-machi, Kanazawa, Ishikawa 920-1192, Japan*
[e]*Institute of Functional Material Chemistry, Faculty of Chemistry, Northeast Normal University, Changchun 130024, P.R. China*

†Electronic supplementary information (ESI) available: Experimental section, IR, NMR, TGA, PXRD, NBO charges, catalytic results. CCDC 2057126 for **1**, 2057132 for **2** and 2057141 for **3_Nb**. For ESI and crystallographic data in CIF or other electronic format see DOI: 10.1039/d1nr04762k

$[M_3O(OOCR)_6(L)_3]^+$.[22] These macrocations have been studied as building blocks of solid materials because a wide choice of metal ions (M^{III}) and ligands (R,L) leads to versatile structures and functions.[23–25] Among the trivalent metal ions (M^{III}), the octahedral Cr^{III} complexes are chemically inert due to the large crystal field stabilization energy of the d^3 electronic configuration,[26] so that $[Cr_3O(OOCR)_6(L)_3]^+$ is stable and would be suitable as a component of PICs with catalytically active POMs. Most importantly, short-range anisotropic interactions such as hydrogen bonds and π–π interactions between the macrocations and catalytically active POMs form unique nano-scale reaction fields in the PICs. In this context, various Keggin-type ($[XM_{12}O_{40}]^{n-}$)[24,25,27,28] and Dawson-type ($[X_2M_{18}O_{62}]^{n-}$)[29,30] POMs (X = P, Si, M = W, Mo, *etc.*) have been incorporated into PICs, while there are no reports on Nb- or Ta-containing POMs.

Based on these considerations, in this work, we report the syntheses, crystal structures, and base catalysis of PICs composed of mono-substituted or tri-substituted Dawson-type Nb/W and Ta/W mixed-addenda POMs with $[Cr_3O(OOCH)_6(H_2O)_3]^+$ (Fig. 1). Compared with polyoxoniobates and polyoxotantalates, Nb/W and Ta/W mixed-addenda POMs are more stable in a broad pH range,[31] which enables them to coexist with the macrocation in the synthetic aqueous solutions. We have utilized POMs with peroxo groups ($[P_2W_{17}(NbO_2)O_{61}]^{7-}$ and $[P_2W_{15}(MO_2)_3O_{59}]^{9-}$, M = Nb or Ta) as starting materials (Fig. 1) because it is well known that peroxo-free Nb/W and Ta/W mixed-addenda POMs tend to aggregate and form a dimer under acidic conditions.[32–34] Therefore, we can expect that the peroxo groups could inhibit dimerization so that the catalytically active Nb and Ta sites can interact with reactant molecules.

Results and discussion

Syntheses

PIC **1** (see below for the formula) was synthesized using the following procedure. $[Cr_3O(OOCH)_6(H_2O)_3](OOCH)\cdot nH_2O$[35] was stirred in dilute aqueous nitric acid (pH = 2) at room temperature until it was fully dissolved. Then, $K_7[P_2W_{17}(NbO_2)O_{61}]\cdot 8H_2O$[36] and KCl were added and dissolved in the solution. The solution was maintained at 277 K for 3 days and green crystals of **1** were obtained. PIC **2** (see below for the formula) was synthesized using a similar procedure using hydrochloric acid instead of nitric acid. The use of the Nb tri-substituted Dawson-type POMs $K_8H[P_2W_{15}(NbO_2)_3O_{59}]\cdot 12H_2O$[36] and $K_5Na_4[P_2W_{15}(TaO_2)_3O_{59}]\cdot 17H_2O$[37] instead of $K_7[P_2W_{17}(NbO_2)O_{61}]\cdot 8H_2O$ gives PIC **3_Nb** and **3_Ta**, respectively (see below for the formulae). PIC **3_Nb** and **3_Ta** crystallized from both hydrochloric acid and nitric acid solutions. IR spectra of the PICs showed characteristic peaks of the macrocation and POMs (Fig. S1–S3†). Elemental analysis and thermogravimetry (Fig. S4–S7†) showed that all PICs contained a macrocation and a POM in a 2 : 1 ratio and K^+ ions compensate the surplus negative charge of the POM. The chemical formulae will be discussed in detail below.

Solid state ^{31}P-MASNMR spectroscopy was utilized to characterize the states of Nb/W and Ta/W mixed-addenda POMs in the PICs (Fig. S8 and S9†). The NMR signals of **1** and **2** can be deconvoluted into two peaks with a 1 : 1 ratio. The peaks at the lower field can be assigned to the P in the half-anion containing Nb, and those at the higher field can be assigned to the other P.[38] In contrast, the NMR signals of **3_Nb** and **3_Ta** can be deconvoluted into two pairs of peaks (Fig. S9a and S9c†), suggesting that the peroxo groups have partially converted to oxo groups in the synthesis (see ESI† for the details).

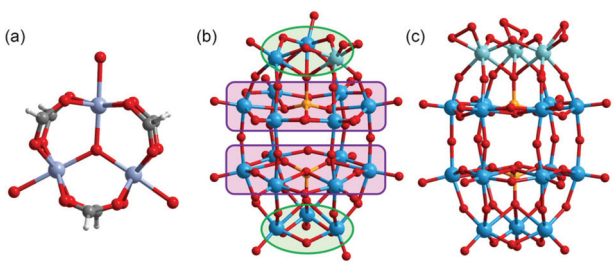

Fig. 1 Molecular structures of (a) $[Cr_3O(OOCH)_6(H_2O)_3]^+$, (b) $[P_2W_{17}(NbO_2)O_{61}]^{7-}$ and (c) $[P_2W_{15}(MO_2)_3O_{59}]^{9-}$ (M = Nb or Ta). Color codes: W: blue; Nb or Ta: cyan; P: orange; O: red; Cr: silver; C: grey, and H: light grey. W atoms at the polar and equatorial sites of the Dawson-type POMs are surrounded by the green ovals and purple rectangles, respectively. W atoms at the polar sites are substituted with Nb or Ta atoms.

Crystal structures of the PICs

The crystallographic data of **1**, **2** and **3_Nb** are summarized in Table S1.† PIC **1** crystallized in the monoclinic space group $P2_1/n$. The substituted Nb atom exists at the polar sites of Dawson-type POMs, while the actual position could not be determined due to the Nb/W substitutional disorder. Single crystal X-ray diffraction (SXRD) analysis of **1** suggests that the peroxo group of the starting material has completely converted to an oxo group, and $[P_2W_{17}NbO_{62}]^{7-}$ is formed, which agrees with the result of solid-state ^{31}P-MASNMR (Fig. S8†). Therefore, **1** can be formulated as $K_5H[Cr_3O(OOCH)_6(H_2O)_3]_2[P_2W_{17}NbO_{62}]\ (NO_3)\cdot 34H_2O$. As shown in Fig. 2a, POMs are arranged at equal intervals forming a triangular lattice in the *ab*-plane. Three K^+ ions are bridged by triangular NO_3^- with K–O distances of 2.79–2.92 Å, and this complex is located on every other centroid of the triangular lattice. The K^+ ions are interlinked by the POMs with K–O distances of 2.66–2.78 Å, resulting in the formation of a 2D-network structure in the *ab*-plane. Fig. 2b shows a column composed of a (A) POM, (B) macrocation, and (C) NO_3^- with an ABCBA packing sequence along the *c*-axis. A K^+ ion bridges (B) and (A) so that the columns are connected to each other *via* K^+ ions in the *ab*-plane forming a honeycomb-like lattice, and 1D-channels with a diameter of *ca.* 13 Å exist along the *c*-axis (Fig. 2c). The void analysis by CSD Mercury[39] indicates that the void volume of **I** is 27.8% of the unit cell (Fig. 2d).

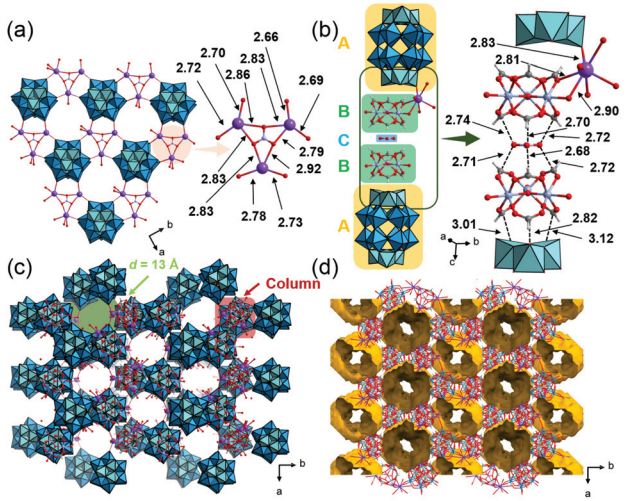

Fig. 2 Crystal structure of $K_5H[Cr_3O(OOCH)_6(H_2O)_3]_2[P_2W_{17}NbO_{62}](NO_3)\cdot 34H_2O$ (**1**). Color codes: W: blue; W/Nb: cyan; P: orange; O: red; Cr: silver; K: violet; C: grey; N: light silver; H: light grey; $[WO_6]$: blue octahedra; $[W/NbO_6]$: cyan octahedra; and $[PO_4]$: orange tetrahedra. (a) Arrangement of a POM, macrocation, and NO_3^- in the *ab*-plane, and a local view of three K^+ ions bridged by a NO_3^- ion. (b) Arrangement of a POM, K^+ ion, and NO_3^- along the *c*-axis. (c and d) Honeycomb-like lattice and 1D channels; void space (in yellow) is depicted with a probe radius of 1.2 Å.

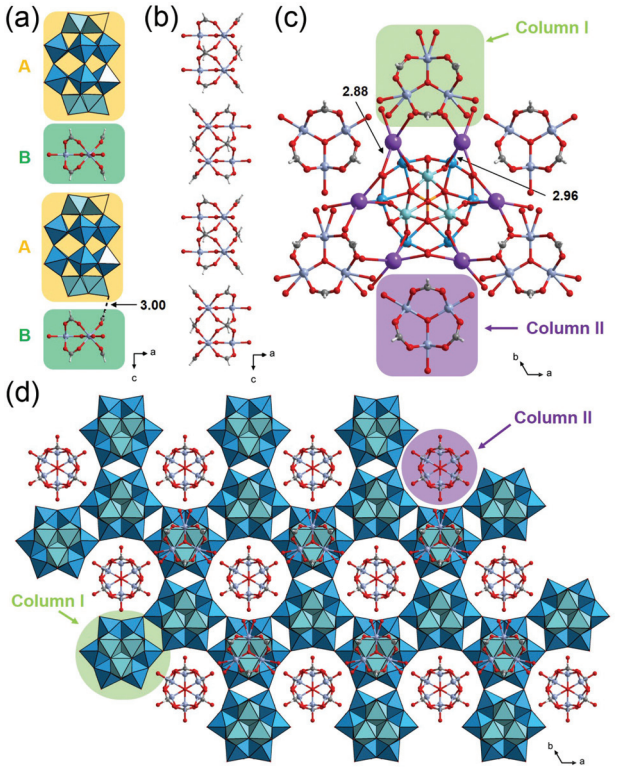

Fig. 3 Crystal structure of $K_5[Cr_3O(OOCH)_6(H_2O)_3]_2[P_2W_{17}NbO_{62}]\cdot 18H_2O$ (**2**). Color codes are the same as Fig. 2. (a) Arrangement of a POM and macrocation in column I. (b) Arrangement of a macrocation in column II. (c) Local view of a POM and the surrounding K^+ ions and macrocations. (d) Honeycomb-like lattice.

PIC **2** is isostructural with the reported PIC composed of $[P_2W_{18}O_{62}]^{6-}$ with a similar hexagonal arrangement $K_4[Cr_3O(H_2O)_3(OOCH)_6]_2[P_2W_{18}O_{62}]\cdot 9.5H_2O$ (**Cr-H-P_2W_{18}**);[29,40] the substitution of W with Nb at the polar sites of the POM leads to a decrease in symmetry, which causes the alteration of the space group from $P6_3/m$ to $P6_3/mmc$. As in the case of **1**, the actual position of Nb could not be determined due to the Nb/W substitutional disorder. The peroxo group of the starting material has completely converted to an oxo group, and $[P_2W_{17}NbO_{62}]^{7-}$ is formed. Therefore, **2** can be formulated as $K_5[Cr_3O(OOCH)_6(H_2O)_3]_2[P_2W_{17}NbO_{62}]\cdot 18H_2O$. The crystal structure of **2** can be described by the assembly of two types of columns I and II. Column I is composed of the (A) POM and (B) macrocation with an ABAB packing sequence along the *c*-axis (Fig. 3a). Column II is composed only of the macrocation, which is positionally disordered with 0.5 occupancy (Fig. 3b). In the *ab*-plane, a POM is surrounded by three macrocations from column I and three macrocations from column II (Fig. 3c). K^+ ions, which are positionally disordered with 1/3 occupancy, bridge the POM and the macrocation with K–O distances of 2.96 and 2.88 Å, respectively. As shown in Fig. 3d, the structure of **2** can be viewed as a honeycomb lattice composed of column I, and column II situates inside the honeycomb.

PIC **3_Nb** crystallized in the trigonal space group $P\bar{3}m1$. Tri-substituted Nb atoms exist at either the top or the bottom polar site of the POM with a ratio of 0.28 : 0.72. In addition, SXRD analysis suggests that about half of the peroxo group of the starting material has converted to an oxo group, which agrees with the results of solid-state ^{31}P-MASNMR (Fig. S9a†). Therefore, **3_Nb** can be formulated as $K_6H[Cr_3O(OOCH)_6(H_2O)_3]_2[P_2W_{15}(NbO_2)_3O_{59}]_{0.5}[P_2W_{15}Nb_3O_{62}]_{0.5}\cdot 17H_2O$. As shown in Fig. 4a, six POMs are interlinked by K^+ ions with K–O distances of 2.94 Å and 2.95 Å, and a six-membered ring is formed. In the six-membered ring, two K^+ ions coordinate to a POM, and these K^+ ions are bridged by a water molecule with a K–O distance of 2.83 Å (Fig. 4a). Macrocations are located at the center of the 6-membered ring and are arrayed along the *c*-axis, and the distances between the μ_3–O of adjacent macrocations are 6.13 and 6.49 Å (Fig. 4b and c). As a result, closed pores, which are surrounded by six macrocations and four POMs, are formed (Fig. 4d and e). The diameter of the closed pore is *ca.* 8 Å and the void analysis indicates that the volume is 8.3% of the unit cell.

The bulk purities of **1**–**3_Nb** were confirmed by powder X-ray diffraction (PXRD) patterns (Fig. S10–S12†); the experimental PXRD patterns were in accordance with those calculated from the crystallographic data. The PXRD pattern of **3_Ta** was analogous to that calculated from the CIF file of **3_Nb**, showing that the two PICs are isostructural (Fig. S13†). In addition, the cell parameters of **3_Ta** were estimated from the PXRD pattern by the Pawley method:[41] a = 16.113(1) Å and c = 25.269(5) Å. The slightly longer *c*-axis may be ascribed to the larger atomic radius of Ta than Nb.

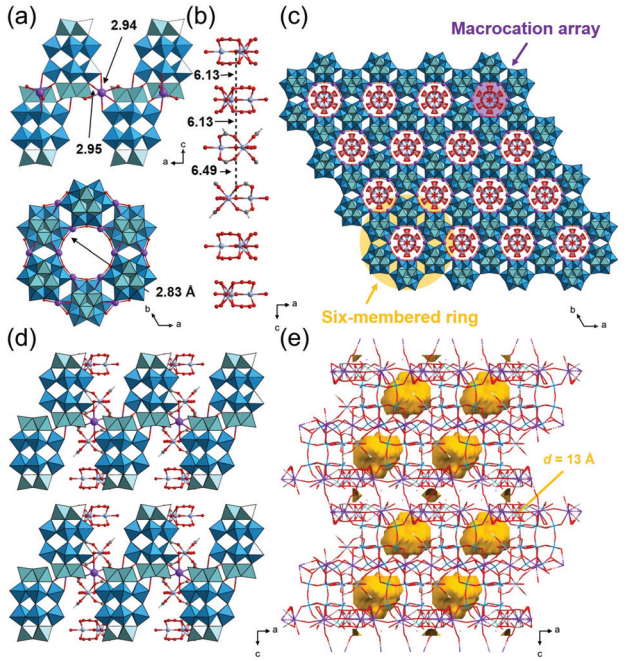

Fig. 4 Crystal structure of $K_6H[Cr_3O(OOCH)_6(H_2O)_3]_2[P_2W_{15}(NbO_2)_3O_{59}]_{0.5}[P_2W_{15}Nb_3O_{62}]_{0.5}\cdot 17H_2O$ (**3_Nb**). Color codes are the same as Fig. 2. (a) Local views of the 6-membered ring; (b) side view of the macrocation array; arrangements of the ionic components (c) in the *ab*-plane and (d) along the *c*-axis; (e) void space (in yellow) is depicted with a probe radius of 1.2 Å.

Catalytic performances in the Knoevenagel condensation

The Knoevenagel condensation is a classic base-catalyzed reaction, which includes nucleophilic addition of an active hydrogen compound to a carbonyl group followed by a dehydration process. We carried out the Knoevenagel condensation of benzaldehyde with ethyl cyanoacetate to investigate the effect of Nb and Ta sites in the PICs on the base catalysis (Scheme 1). The reaction conditions (solvent, temperature, time, and mole ratio) were optimized (Table S2†), and the results are summarized in Table 1 (see Table S3† for full results). The product (ethyl α-cyanocinnamate) yield in the absence of a catalyst was 9% (entry 1). PICs **1** and **2** exhibited product yields of 18% and 29% after 6 h (entries 2 and 3, Fig. 5). However, the PXRD patterns of **1** and **2** indicated that amorphous phases and/or different structures are generated under reaction conditions, which is a drawback as a solid catalyst (Fig. S10 and S11†). As expected, **3_Nb** showed a product yield of 40% after 1 h, which reached 78% after 6 h (entry 4, Fig. 5); the product yield is comparable to those of highly basic POMs as solid catalysts and higher than some typical metal oxides and zeolites (Table S4†). The product selectivity was maintained at 99% throughout the reaction with no obvious by-products (Fig. S14 (GC chart) and Fig. S15 (^{1}H-NMR)†). As shown in Fig. 5, the reaction completely stopped upon the removal of **3_Nb**, and no obvious leaching in the filtrate was detected by AAS (less than 1% based on Cr). These results show that the observed catalysis is truly heterogeneous. Moreover, **3_Nb** is easily recovered from the reaction mixture by simple filtration and washing with ethanol and can be reused at least twice without a significant loss in the yield or selectivity (entries 5 and 6). The PXRD patterns and cell parameters of **3_Nb** did not show obvious changes under the reaction conditions (Fig. S12c and S12d†), which confirms the durability as a solid catalyst. PIC **3_Ta** exhibited a product yield of 29% after 1 h, which reached 82% after 6 h (entry 7, Fig. 5). The product selectivity was maintained at 99%

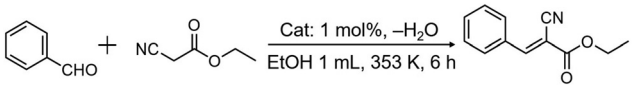

Scheme 1 Knoevenagel condensation of benzaldehyde and ethyl cyanoacetate.

Table 1 Catalytic results of various catalysts in the Knoevenagel condensation reaction[a]

Entry	Catalyst	Conv./%	Yield[b]/%	Selec.[c]/%
1	None	35	9	25
2	**1**	46	18	39
3	**2**	51	29	57
4	**3_Nb**[d]	79	78	99
5	**3_Nb** (2nd run)	79	78	99
6	**3_Nb** (3rd run)	75	70	93
7	**3_Ta**[d]	83	82	99
8	**3_Ta** (2nd run)	83	82	99
9	**3_Ta** (3rd run)	81	77	95
10	**Cr-H-P_2W_{18}**[e]	45	21	47

[a] Reaction conditions: 0.01 mmol catalyst, 1.0 mmol benzaldehyde, 1.0 mmol ethyl cyanoacetate, 10 mg biphenyl (internal standard), and 1 mL ethanol. [b] Yield of ethyl α-cyanocinnamate. [c] Selectivity to ethyl α-cyanocinnamate. [d] Since the particle size of solid catalysts may affect the catalysis, the solids were ground and passed through a 150-mesh sieve. [e] Catalyst dissolved in the reaction solution.

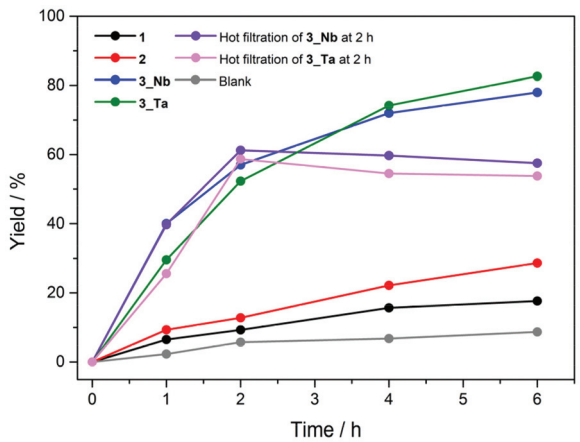

Fig. 5 Time courses of the Knoevenagel condensation catalyzed by **1** (black), **2** (red), **3_Nb** (blue), and **3_Ta** (green), and the blank test (gray) and that after removal of **3_Nb** (purple) or **3_Ta** (pink).

(Fig. S14 (GC) and Fig. S15 (^{1}H-NMR)†). PIC **3_Ta** showed a catalytic activity similar to that of **3_Nb** (Fig. 5), can be reused at least twice without significant changes in the structure (entries 8 and 9, Fig. S13c and S13d†), and showed no leaching. As a reference, the reaction was carried out with the non-substituted PIC (**Cr-H-P$_2$W$_{18}$**, entry 10), which showed a low product yield, indicating that the incorporation of Nb or Ta is crucial to the base catalysis. Note that the catalytic performances of physical mixtures of the macrocation and POM (entries 6–8 in Table S3†) were much inferior, suggesting the importance of the nanoscale reaction field. PIC **3_Nb** and **3_Ta** can also catalyze the Knoevenagel condensation of benzaldehyde and malononitrile (Table S5†), and both reached high yields (99% for **3_Nb** and 96% for **3_Ta**), which are comparable to those of highly basic POMs as catalysts.[10,12,13,42–44]

Among the PICs, the product yields decreased in the order of **3_Ta** (82%) ≈ **3_Nb** (78%) > **2** (29%) > **1** (18%). It is generally understood that the void space or porosity of solid catalysts, where the reaction takes place, is one of the important keys in heterogeneous reactions. However, the porosity decreases in the order of **1** (28.9%) > **2** (*ca.* 11%)‡ ≈ **3_Nb**, **3_Ta** (8.7%), which shows no relationship with the catalysis. The water adsorption isotherms of **1–3** at 298 K (Fig. S16†) show that the amounts of water adsorbed at 2.85 kPa or P/P_0 = 0.9 decrease in the order of **1** (33 mol mol^{-1}, *i.e.*, the amount of water in mol per mol of PIC) > **2** (13) ≈ **3_Nb** (12) ≈ **3_Ta** (10), which is in line with the porosity judged from the crystal structures. The porosity is further characterized by CO_2 adsorption isotherms at 268 K (Fig. S17†), which show the same order of **1** (1.3) > **2** (0.6) ≈ **3_Nb** (0.7) ≈ **3_Ta** (0.6) at 90 kPa.§ These results suggest that the local structure of PICs rather than porosity may be affecting the catalytic activity. In fact, in the crystal structure of **3_Nb**, the terminal oxygen atoms of the Nb sites are exposed to the voids (Fig. 6), which allows the reactants to directly contact the active sites. On the other hand, in the crystal structures of **1** and **2**, the polar sites of the POM are in close contact with the macrocation, so that the active sites are probably blocked (Fig. 6). This kind of steric effect has been also observed in homogeneous Knoevenagel reactions.[45]

Basicity of the oxygen atoms of [NbO$_6$] and [TaO$_6$] sites

Previous studies indicate that the basic oxygen (O) atoms of a POM serve as active-sites for the Knoevenagel reaction and that the basicity of the O atom strongly correlates with the negative charge.[12,13] In order to study the basicity of the Nb- and Ta-substituted POMs, theoretical calculations were performed by the density functional theory (DFT) method

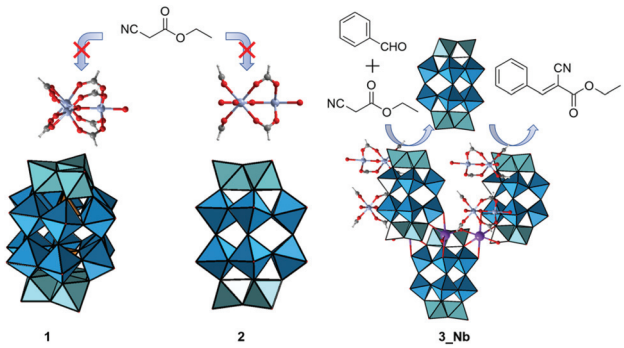

Fig. 6 Schematic illustration of the possible steric effects in **1**, **2**, and **3_Nb**.

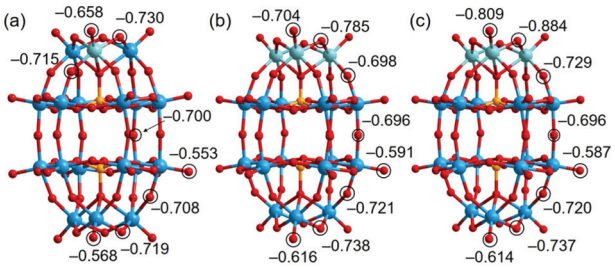

Fig. 7 Calculated NBO charges of oxygen atoms in (a) $[P_2W_{17}NbO_{62}]^{7-}$ in **2**, (b) $[P_2W_{15}Nb_3O_{62}]^{9-}$ in **3_Nb**, and (c) $[P_2W_{15}Ta_3O_{62}]^{9-}$ in **3_Ta**.

(Tables S6–S9†). Fig. 7 shows the optimized molecular structures and natural bond orbital (NBO) charges of the O atoms in $[P_2W_{17}NbO_{62}]^{7-}$, $[P_2W_{15}Nb_3O_{62}]^{9-}$, and $[P_2W_{15}Ta_3O_{62}]^{9-}$. The terminal ($O_t$(W)) and bridging (W–$O_b$–W) O atoms of $[WO_6]$ in $[P_2W_{17}NbO_{62}]^{7-}$ have NBO charges ranging from −0.553 to −0.568 and −0.700 to −0.719, respectively. The terminal O atom of $[NbO_6]$ in $[P_2W_{17}NbO_{62}]^{7-}$ (O_t(Nb)) has an NBO charge of −0.658, and those of the bridging O atoms between $[WO_6]$ and $[NbO_6]$ (O_b(W–O_b–Nb)) range from −0.715 to −0.730. For $[P_2W_{15}Nb_3O_{62}]^{9-}$, the O atoms of $[NbO_6]$ show higher negative NBO charges (−0.704 for O_t(Nb) and −0.785 for O_b(Nb–O_b–Nb)) than those of $[WO_6]$ (the highest negative values are −0.616 and −0.738 for O_t(W) and O_b(W–O_b–W), respectively). The negative NBO charges of O atoms of $[TaO_6]$ in $[P_2W_{15}Ta_3O_{62}]^{9-}$ (−0.809 for O_t(Ta) and −0.884 for O_b(Ta–O_b–Ta)) are higher than those of $[NbO_6]$ in $[P_2W_{15}Nb_3O_{62}]^{9-}$. In addition, DFT calculations were carried out for the non-substituted $[P_2W_{18}O_{62}]^{6-}$. As shown in Fig. S18,† the NBO charges of the terminal O atoms of $[WO_6]$ in $[P_2W_{18}O_{62}]^{6-}$ are −0.546 and −0.538, for the polar and equatorial positions, respectively. The negative charges of the O atoms of Nb/Ta-substituted POMs (−0.658 to −0.809 for the polar positions and −0.553 to −0.591 for the equatorial positions) were much higher than those of the non-substituted POM. The results on NBO charges suggest that the basicity would be in the order of $[P_2W_{18}O_{62}]^{6-}$ < $[P_2W_{17}NbO_{62}]^{7-}$ < $[P_2W_{15}Nb_3O_{62}]^{9-}$ < $[P_2W_{15}Ta_3O_{62}]^{9-}$ for the POMs and **1**, **2** < **3_Nb** < **3_Ta** for the PICs. However, the catalytic activities were in the order of **1** < **2** ≪ **3_Nb** ≈ **3_Ta**

‡The void volume of **2** cannot be evaluated with accuracy because of the positional disorder of the macrocation. The void volume of **2** is calculated as 0.7% with the disordered macrocation and 21.1% without the disordered macrocation. Therefore, *ca.* 11% is an average of the two values.

§There is a large discrepancy between the amounts of water and CO_2 adsorption because of the difference in the saturated vapor pressure of the gaseous adsorbates at measurement temperatures (*i.e.*, P_0 = 3.167 kPa for water at 298 K and P_0 = 3.03 × 10^3 kPa for CO_2 at 268 K).

(Table 1). These results clearly indicate that not only basicity but also the steric effect, as illustrated in Fig. 6, affects the base catalysis.

The accessibility of the basic sites in the PICs was characterized by *in situ* IR spectroscopy with methanol, which is one of the smallest and simplest basic probe molecules. Fig. S19† shows the difference spectra of methanol adsorbed on the PICs at 298 K. PICs **1–3** exhibit broad bands between 3400 and 3600 cm^{-1}, which can be assigned to the ν(OH) of methanol.[46] In addition, the spectra show bands at 2945 cm^{-1} and 2838 cm^{-1}, which can be assigned to the asymmetric and symmetric CH_3 stretching vibration modes, respectively.[42] The positions of the bands suggest that methanol is molecularly adsorbed on the PICs. In contrast, **Cr-H-P_2W_{18}** shows no signals due to methanol. Therefore, methanol probably adsorbs on the [NbO_6] and [TaO_6] sites, and not on the [WO_6] sites, highlighting the importance of accessible basic [NbO_6] or [TaO_6] sites to attain high catalytic activity in the Knoevenagel reaction catalyzed by PICs. Furthermore, the methanol desorption behaviors of **3_Nb** and **3_Ta** were almost identical (Fig. S20†), indicating that the interactions between methanol and **3_Nb** or **3_Ta** are alike, which is in line with the similar catalytic activities.

Conclusions

For the first time, Nb- and Ta-containing porous ionic crystals (PICs) composed of Dawson-type Nb/W mixed-addenda POMs with oxo-centered trinuclear Cr^{III} carboxylates and potassium ions as counter cations were reported. The PICs with Nb or Ta tri-substituted POMs exhibited high yields and selectivities in the Knoevenagel condensation as reusable solid base catalysts. The high catalytic activities can be ascribed to a synergetic effect of high basicity of [Nb_3O_{13}] or [Ta_3O_{13}] and the exposure of these sites to the pore surface. These findings based on the composition–structure–function relationships show that Nb- and Ta-containing PICs can serve as platforms for rational designing of heterogeneous base catalysts. Since these PICs can adsorb CO_2 under ambient conditions, our next aim is to look into CO_2 fixation reactions.

Author contributions

Z.W. and N.O. performed the syntheses and characterization of the compounds; Z.W. carried out the SXRD measurements and analysis; T.K. carried out the XRF measurements; Y.K. carried out the *in situ* IR measurements; Y.G. and L.Y. carried out the DFT calculations; Z.W., N.O., and S.U. wrote the manuscript. S.U. conceived and designed the project. All authors discussed the results and commented on the manuscript.

Conflicts of interest

There are no conflicts to declare.

Acknowledgements

This work was supported by the JSPS Grants-in-Aid for Scientific Research from MEXT of Japan (JP20H02750 and JP21K14639), the International Network on Polyoxometalate Science at Hiroshima University, and the JSPS Core-to-Core program. Prof. T. Ito (Tokai University) is acknowledged for obtaining the SXRD data of **3_Nb**. Prof. T. Uemura (Univ. of Tokyo) is acknowledged for providing access to the X-ray fluorescence instrument. Prof. M. Matsuo and Dr K. Shozugawa (Univ. of Tokyo) are acknowledged for providing access to the ICP-OES instrument.

Notes and references

1 M. T. Pope and A. Müller, *Angew. Chem., Int. Ed. Engl.*, 1991, **30**, 34–48.
2 C. L. Hill, *Chem. Rev.*, 1998, **98**, 1–2.
3 L. Vilà-Nadal and L. Cronin, *Nat. Rev. Mater.*, 2017, **2**, 17054.
4 S. Wang and G. Yang, *Chem. Rev.*, 2015, **115**, 4893–4962.
5 Q. Y. Chen, C. R. Shen and L. He, *Acta Crystallogr., Sect. C: Struct. Chem.*, 2018, **74**, 1182–1201.
6 J. J. Walsh, A. M. Bond, R. J. Forster and T. E. Keyes, *Coord. Chem. Rev.*, 2016, **306**, 217–234.
7 K. Kamata and K. Sugahara, *Catalysts*, 2017, **7**, 1–24.
8 T. Kimura, K. Kamata and N. Mizuno, *Angew. Chem., Int. Ed.*, 2012, **51**, 6700–6703.
9 T. Kimura, H. Sunaba, K. Kamata and N. Mizuno, *Inorg. Chem.*, 2012, **51**, 13001–13008.
10 K. Sugahara, T. Kimura, K. Kamata, K. Yamaguchi and N. Mizuno, *Chem. Commun.*, 2012, **48**, 8422–8424.
11 Y. Ono and H. Hattori, *Solid base catalysis*, Springer-Verlag Berlin Heidelberg, 2011.
12 Q. Xu, Y. Niu, G. Wang, Y. Li, Y. Zhao, V. Singh, J. Niu and J. Wang, *Mol. Catal.*, 2018, **453**, 93–99.
13 W. Ge, X. Wang, L. Zhang, L. Du, Y. Zhou and J. Wang, *Catal. Sci. Technol.*, 2016, **6**, 460–467.
14 M. Nyman, *Dalton Trans.*, 2011, **40**, 8049–8058.
15 H. L. Wu, Z. M. Zhang, Y. G. Li, X. L. Wang and E. B. Wang, *CrystEngComm*, 2015, **17**, 6261–6268.
16 A. Misra, K. Kozma, C. Streb and M. Nyman, *Angew. Chem., Int. Ed.*, 2020, **59**, 596–612.
17 O. Sadeghi, L. N. Zakharov and M. Nyman, *Science*, 2015, **347**, 1359–1362.
18 Y. Ren, M. Wang, X. Chen, B. Yue and H. He, *Materials*, 2015, **8**, 1545–1567.
19 S. Uchida, *Chem. Sci.*, 2019, **10**, 7670–7679.
20 S. Uchida, T. Okunaga, Y. Harada, S. Magira, Y. Noda, T. Mizuno and T. Tachikawa, *Nanoscale*, 2019, **11**, 5460–5466.
21 N. Ogiwara, M. Tomoda, S. Miyazaki, Z. Weng, H. Takatsu, H. Kageyama, T. Misawa, T. Ito and S. Uchida, *Nanoscale*, 2021, **13**, 8049–8057.
22 Y. Shimoyama and S. Uchida, *Chem. Lett.*, 2021, **50**, 21–30.

23 A. Vimont, J.-M. Goupil, J.-C. Lavalley, M. Daturi, S. Surblé, C. Serre, F. Millange, G. Férey and N. Audebrand, *J. Am. Chem. Soc.*, 2006, **128**(10), 3218–3227.
24 R. Kawahara, K. Niinomi, J. N. Kondo, M. Hibino, N. Mizuno and S. Uchida, *Dalton Trans.*, 2016, **45**, 2805–2809.
25 T. Yamada, K. Kamata, E. Hayashi, M. Hara and S. Uchida, *ChemCatChem*, 2019, **11**, 3743–3747.
26 M. Weller, T. Overton, J. Rourke and F. Armstrong, *Shriver-Atkins Inorganic Chemistry*, Oxford University Press, Oxford, 6th edn, 2014.
27 S. Uchida, M. Hashimoto and N. Mizuno, *Angew. Chem., Int. Ed.*, 2002, **41**, 2814–2817.
28 S. Uchida, R. Kawamoto and N. Mizuno, *Inorg. Chem.*, 2006, **45**, 5136–5144.
29 S. Uchida, R. Kawamoto, T. Akatsuka, S. Hikichi and N. Mizuno, *Chem. Mater.*, 2005, **17**, 1367–1375.
30 S. Hitose and S. Uchida, *Inorg. Chem.*, 2018, **57**, 4833–4836.
31 D. Zhang, Z. Liang, S. Xie, P. Ma, C. Zhang, J. Wang and J. Niu, *Inorg. Chem.*, 2014, **53**, 9917–9922.
32 G.-S. Kim, H. Zeng, W. A. Neiwert, J. J. Cowan, D. VanDerveer, C. L. Hill and I. A. Weinstock, *Inorg. Chem.*, 2003, **42**, 5537–5544.
33 R. G. Finke and M. W. Droege, *J. Am. Chem. Soc.*, 1984, **106**, 7274–7277.
34 K. Nomiya, M. Kaneko, N. C. Kasuga, R. G. Finke and M. Pohl, *Inorg. Chem.*, 1994, **33**, 1469–1472.
35 M. K. Johnson, D. B. Powell and R. D. Cannon, *Spectrochim. Acta*, 1981, **37**, 995–1006.
36 J. Gong, Y. Chen, L. Y. Qu and L. Qin, *Polyhedron*, 1996, **15**, 2273–2277.
37 S. Li, S. Liu, S. Liu, Y. Liu, Q. Tang, Z. Shi, S. Ouyang and J. Ye, *J. Am. Chem. Soc.*, 2012, **134**, 19716–19721.
38 D. A. Judd, J. H. Nettles, N. Nevins, J. P. Snyder, D. C. Liotta, J. Tang, J. Ermolieff, R. F. Schinazi and C. L. Hill, *J. Am. Chem. Soc.*, 2001, **123**, 886–897.
39 C. F. Macrae, I. Sovago, S. J. Cottrell, P. T. A. Galek, P. McCabe, E. Pidcock, M. Platings, G. P. Shields, J. S. Stevens, M. Towler and P. A. Wood, *J. Appl. Crystallogr.*, 2020, **53**, 226–235.
40 X. Zhang, W. You, Z. Zhu, L. Dang, Z. Sun and X. Zheng, *Chem. Res. Chin. Univ.*, 2007, **23**, 8–13.
41 G. S. Pawley, *J. Appl. Crystallogr.*, 1981, **14**, 357–361.
42 A. Yoshida, S. Hikichi and N. Mizuno, *J. Organomet. Chem.*, 2007, **692**, 455–459.
43 A. Davoodnia, *Synth. React. Inorg. Met.-Org. Chem.*, 2012, **42**, 1022–1026.
44 S. Zhao, Y. Chen and Y.-F. Song, *Appl. Catal., A*, 2014, **475**, 140–146.
45 S. Hayashi, S. Yamazoe and T. Tsukuda, *J. Phys. Chem. C*, 2020, **124**, 10975–10980.
46 S. Kanai, I. Nagahara, Y. Kita, K. Kamata and M. Hara, *Chem. Sci.*, 2017, **8**, 3146–3153.